

Electronic Supplementary Information for:

# Compositional Heterogeneity in $\text{Cs}_y\text{FA}_{1-y}\text{Pb}(\text{Br}_x\text{I}_{1-x})_3$ Perovskite Films and its Impact on Phase Behavior

Julien Barrier<sup>1,2,\*</sup> Rachel E. Beal<sup>1,3,\*</sup> Aryeh Gold-Parker<sup>1,4</sup> Julian A. Vigil<sup>1,5</sup>  
Eli Wolf<sup>6,7</sup> Louis Waquier<sup>1,2</sup> Nicholas J. Weadock<sup>1,7</sup> Zihan Zhang<sup>8</sup>  
Laura T. Schelhas<sup>9</sup> Ana Flavia Nogueira<sup>10</sup> Michael D. McGehee<sup>7,9</sup>  
Michael F. Toney<sup>7†</sup>

<sup>1</sup> SSRL Materials Science Division, SLAC National Accelerator Laboratory, Menlo Park CA 94025, USA

<sup>2</sup> École Supérieure de Physique et de Chimie Industrielles de la Ville de Paris - ESPCI Paris, 75005 Paris, France

<sup>3</sup> Department of Materials Science and Engineering, Stanford University, Stanford CA 94305, USA

<sup>4</sup> Department of Chemistry, Stanford University, Stanford CA 94305

<sup>5</sup> Department of Chemical Engineering, Stanford University, Stanford CA 94305, USA

<sup>6</sup> Department of Applied Physics, Stanford University, Stanford, CA 94305, USA

<sup>7</sup> Department of Chemical and Biological Engineering, University of Colorado Boulder, Boulder, CO 80309, USA

<sup>8</sup> Physics Department, University of Colorado Boulder, Boulder, CO 80309, USA

<sup>9</sup> National Renewable Energy Laboratory, Golden, CO 80401, USA

<sup>10</sup> Institute of Chemistry, University of Campinas, Campinas SP 13083-970 São Paulo, Brazil

## Supplementary section 1: Tolerance factors

We calculate  $\tau_G$  as function of composition in fig. S1a and plot this for the  $\text{Cs}_y\text{FA}_{1-y}\text{Pb}(\text{Br}_x\text{I}_{1-x})_3$  compositions studied in this work as well as those reported in Beal et al.[1]. The phase behavior we observe is consistent with the Goldschmidt tolerance factor, but we do not observe a distinct cutoff value above which the materials are cubic and below which they are tetragonal. In fig. S1a and S1b, we highlight that for  $\tau_G$  around 0.976, both crystal structures are observed. Note that  $\tau_G$  calculations for hybrid perovskites are complicated by the fact that it is difficult to determine the radii of the organic cations [2]. Bond lengths between the organic cations and the halide ions may also vary based on molecular orientation and may be different from the rigid sphere assumption implicit in  $\tau_G$  (refs [2, 3, 4]). Rather than redefining the ionic radii, Bartel *et al.* used the *SISSO* (sure independence screening and sparsifying operator) method to identify a modified tolerance factor  $\tau_C = \frac{r_X}{r_B} - n_A \left( n_A - \frac{r_A/r_B}{\log(r_A/r_B)} \right)$ , where  $r_i$  are still the Shannon radii and  $n_A$  is the oxidation state of the A-site cation [5].  $\tau_C$  was trained on experimental data and predicts the stability of 576  $ABX_3$  (and  $A_2B'BX_6$ ) compositions in the perovskite (or double perovskite) crystal structure at room temperature with > 90% accuracy [6]. Unlike  $\tau_G$ , the probability that a material is perovskite varies monotonically with  $\tau_C$ , which predicts that compositions with  $\tau_C < 4.18$  will be stable in the perovskite crystal structure [6]. We note that for the  $\text{Cs}_y\text{FA}_{1-y}\text{Pb}(\text{Br}_x\text{I}_{1-x})_3$  compositions studied here,  $n_A = 1$ , so the equation simplifies to  $\tau_C = \frac{r_X}{r_B} + \frac{r_A/r_B}{\log(r_A/r_B)} - 1$ .

\*These authors contributed equally.

†Correspondance for this work should be addressed to M.F. Toney [michael.toney@colorado.edu](mailto:michael.toney@colorado.edu)

While  $\tau_G$  was not explicitly trained to predict crystal structure within the perovskite classification, we find that it does have a specific value that discriminates between the cubic and tetragonal perovskite crystal structures for the  $\text{Cs}_y\text{FA}_{1-y}\text{Pb}(\text{Br}_x\text{I}_{1-x})_3$  compositions studied here. Figure S1c shows a contour plot for this corrected tolerance factor, and fig. S1d shows that unlike  $\tau_G$ , there is a distinct cutoff of  $\tau_C = 3.55$  above which materials are cubic and below which they are tetragonal.

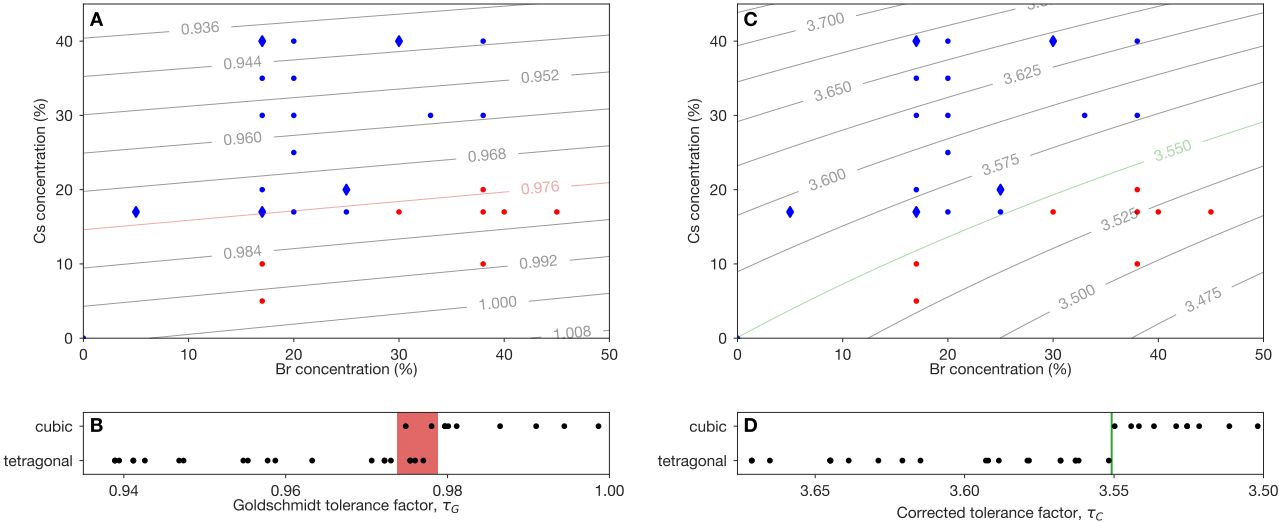


**Figure S1:** Comparison of the stable phase at room temperature and tolerance factors. (A) Contour plot of the Goldschmidt tolerance factor  $\tau_G$  as a function of Cs and Br substitution. Compositions found to be cubic are plotted in blue, and compositions where tetragonal phase is present are plotted in red. Dots represent data extracted from Beal *et al.* [1]. (B) Classifications of the room-temperature crystallographic phase against the Goldschmidt tolerance factor classifier. (C & D) The same treatment as in (A & B), except with the tolerance factor from Bartel *et al.* [6].

## Supplementary section 2: Fit of the Bragg Peaks

For a given composition, we fit the Bragg peaks with a Voigt function and a quadratic background using a least squares method. To optimize the fit, we used the following procedure:

1. We started with the lowest temperature; we fit the data with a Voigt plus a quadratic background for the  $t(110)$ ,  $t(200)$ ,  $t(201)$  and  $t(210)$  peaks around  $q$  values of  $\sim 1 \text{ \AA}^{-1}$ ,  $1.4 \text{ \AA}^{-1}$ ,  $1.7 \text{ \AA}^{-1}$  and  $1.6 \text{ \AA}^{-1}$ , respectively. The Voigt function center, width and other parameters are collected from the fitted peaks and from the quadratic background.
2. We then fit successively higher temperature data. For each incrementally higher temperature, we initialise the fit with the parameters extracted from the prior (lower) temperature. The peak center is allowed to vary from  $q[LT] - 0.02 \text{ \AA}^{-1}$  to  $q[LT] + 0.02 \text{ \AA}^{-1}$ , where  $q[LT]$  is the peak center at the lower temperature. The width is allowed to float  $\pm 30\%$  from the lower temperature fit. The quadratic background shape is fixed but we allow a multiplicative offset parameter to vary. This variation in overall background intensity reflects small changes in background.

This allows us to retrieve the integrated intensities of the 4 peaks for the whole temperature range. We observed that the widths of the  $t(110)$ ,  $t(200)$  and  $t(201)$  peaks narrow slightly with increasing temperature (about 2% per degree), which we attribute in the tetragonal phase to a reduction of the  $c$  over a ratio and in the cubic phase to reduced nonuniform strain.

### 2.1 chi-squared analysis

The  $\chi^2$  analysis allows us to distinguish the  $t(210)$  peak from background. At each temperature, we examine the  $t(210)$  peak within a small  $q$  range of  $\pm 0.06 \text{ \AA}^{-1}$  about the peak position. We compare the  $\chi^2$  statistic for two hypotheses: no peak (H0) and presence of the  $t(210)$  peak (H1). The intensities for these two hypotheses are then given by: a quadratic function (H0) and a small Voigt peak over a quadratic background (H1). We show here the analysis with the example of composition  $\text{Cs}_y\text{FA}_{1-y}\text{Pb}(\text{Br}_x\text{I}_{1-x})_3$  with  $x = 20$ ,  $y = 25$ . For H0, we fit only the background with a quadratic function of the form  $aq^2 + bq + c$ . For H1, we fix the Voigt to the value obtained in the best fit. As a result, we vary the three quadratic parameters ( $a$ ,  $b$  and  $c$ ) for the two hypothesis, allowing comparison of the  $\chi^2$ , which are calculated with Python's `lmfit`[7] as the non-normalized sum of the residuals. At the temperature where the  $t(210)$  peak vanishes, we expect the fits with H0 and H1 hypotheses to have equivalent  $\chi^2$ . This test defines the temperature  $T_0$  where the tetragonal peak intensity goes to zero, and the result of this is shown in table 1 (main text). The  $\chi^2$  values for  $\text{Cs}_{0.25}\text{FA}_{0.75}\text{Pb}(\text{Br}_{0.2}\text{I}_{0.8})_3$  are presented in figure S2. Examples of fits with the two hypothesis H0 and H1 for the  $t(210)$  peak above and below the temperature  $T_0$  are shown in figure S3 as a function of temperature. Our conclusion is that the  $t(210)$  peak goes to zero (within our error bars) at about  $56^\circ\text{C}$  (between  $55^\circ\text{C}$  and  $57.6^\circ\text{C}$ ). The intensity of the peaks as a function of the temperature are presented in figure 3a (main text). Our analysis for  $[x = 5, y = 17]$ ,  $[x = 17, y = 17]$  and  $[x = 30, y = 40]$  is similar to that described above. For the composition  $[x = 17, y = 40]$ , we observe a background peak above the quadratic background with a small intensity, appearing at higher  $q$  than the  $t(210)$  peak, and so we model the background with a quadratic function and a Voigt function for this particular composition.

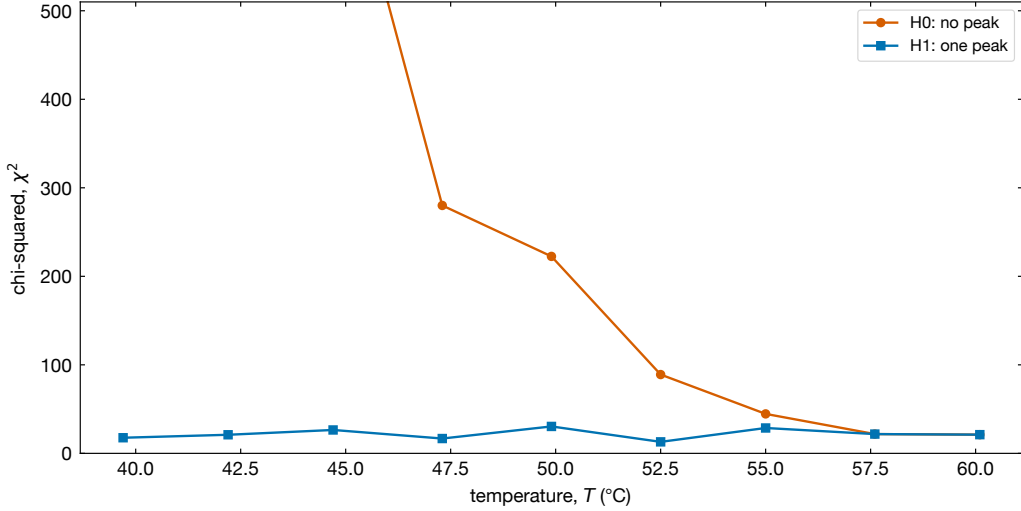


**Figure S2:** Chi squares (truncated on the range 0-500) for the fit of a background at  $q = 1.6 \text{ \AA}^{-1}$  (expected  $t(210)$  Bragg peak) with no peak (orange circles), with one peak of known intensity (purple squares) or with two peaks of known intensity (blue triangles) versus temperature for the perovskite of composition  $\text{Cs}_{0.25}\text{FA}_{0.75}\text{Pb}(\text{Br}_{0.2}\text{I}_{0.8})_3$ .

### Supplementary section 3: Calculation of the Tilt Angle

Here we explain how the tilt angle was determined from the diffraction peak intensities. Note that we define the tilt angle for one  $\text{PbX}_6$  octahedron, with Pb taken as the center and the angle relative to the cubic phase atomic position of the halide.

#### 3.1 Tilt angle vs intensity

The tetragonal phase (space group  $P4/mbm$ ) corresponds to a rotation of the  $\text{PbX}_6$  octahedra around the  $c$  axis. The calculation below relates the intensity of the  $t(210)$  peak to the octahedral tilt angle. The results of these calculations are presented in figure 3 (main text). The intensity of a peak can be written as:

$$I_{hkl} = A \cdot |F_{hkl}|^2 \cdot p \cdot \left( \frac{1 + \cos^2 2\theta}{\sin^2 \theta \cos \theta} \right) \quad (\text{S1})$$

where  $F_{hkl}$  is the structure factor,  $p$  is the multiplicity,  $\theta$  is the Bragg angle and  $A$  is a proportionality factor independent of  $hkl$  [8].

$F_{hkl}$  can be calculated with the following formula:

$$F_{hkl} = \sum_{\text{sites}} (f_{\text{Pb}} e^{-M_{\text{Pb}}} e^{2j\pi\mathbf{q}\cdot\mathbf{r}_{\text{Pb}}} + f_{\text{A}} e^{2j\pi\mathbf{q}\cdot\mathbf{r}_{\text{A}}} + f_{\text{X}} e^{2j\pi\mathbf{q}\cdot\mathbf{r}_{\text{X}}}) \quad (\text{S2})$$

With, in the tetragonal system:  $\mathbf{q} = \begin{bmatrix} h \\ k \\ l \end{bmatrix}$  and  $\mathbf{r}_{\text{Pb}} \in \left\{ \begin{bmatrix} \frac{1}{2} \\ 0 \\ \frac{1}{2} \end{bmatrix}, \begin{bmatrix} 0 \\ \frac{1}{2} \\ \frac{1}{2} \end{bmatrix} \right\}$ ,  $\mathbf{r}_{\text{A}} \in \left\{ \begin{bmatrix} 0 \\ 0 \\ 0 \end{bmatrix}, \begin{bmatrix} \frac{1}{2} \\ \frac{1}{2} \\ 0 \end{bmatrix} \right\}$ ,

and  $\mathbf{r}_{\text{X}} \in \left\{ \begin{bmatrix} 0.5 \\ 0 \\ 0 \end{bmatrix}, \begin{bmatrix} 0 \\ 0.5 \\ 0 \end{bmatrix}, \begin{bmatrix} \frac{1-\cos(\frac{\pi}{4}-t)}{2\sqrt{2}} \\ \frac{\sin(\frac{\pi}{4}-t)}{2\sqrt{2}} \\ \frac{1}{2} \end{bmatrix}, \begin{bmatrix} \frac{1+\cos(\frac{\pi}{4}+t)}{2\sqrt{2}} \\ \frac{\sin(\frac{\pi}{4}-t)}{2\sqrt{2}} \\ \frac{1}{2} \end{bmatrix}, \begin{bmatrix} \frac{\sin(\frac{\pi}{4}+t)}{2\sqrt{2}} \\ \frac{1+\cos(\frac{\pi}{4}+t)}{2\sqrt{2}} \\ \frac{1}{2} \end{bmatrix}, \begin{bmatrix} 1 - \frac{\sin(\frac{\pi}{4}-t)}{2\sqrt{2}} \\ 1 - \frac{1+\cos(\frac{\pi}{4}+t)}{2\sqrt{2}} \\ \frac{1}{2} \end{bmatrix} \right\}$ . where the

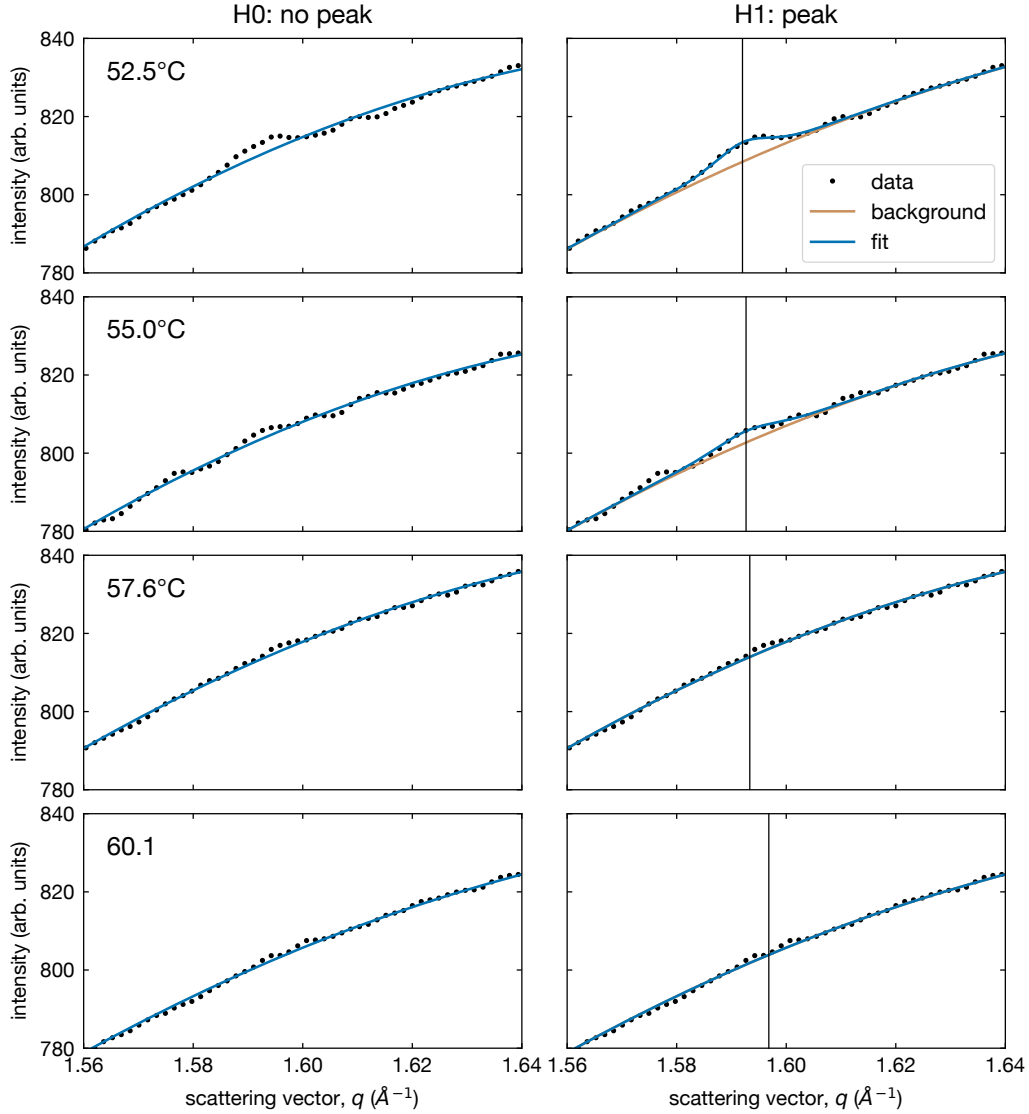


**Figure S3:** Fits of  $I(q)$  diffraction pattern for composition 25-20 around  $q = 1.6 \text{ \AA}^{-1}$  (corresponding to the Bragg peak  $t(210)$ ) with hypothesis H0 (no peak, left), H1 (Voigt with known intensity over a quadratic background, right), for four temperatures around expected tetragonal-to-cubic phase transition. The fits correspond to the chi-square analysis presented in Figure S2. The black dots show the raw data, the brown line the background and the blue line the fitted background plus the Voigt peak. Vertical lines show the center of the peak.

tilt angle is denoted  $t$ . The atomic factors are taken as:  $f_A = [Cs] \times f_{Cs}e^{-M_{Cs}} + (1 - [Cs]) \times [2 \cdot f_Ce^{-M_C} + f_Ne^{-M_N}]$  (we assume that the atomic form factors of the hydrogen atoms of the FA molecules are negligible compared to those of the carbon and nitrogen atoms).

$$f_X = [Br] \times f_{Br}e^{-M_{Br}} + (1 - [Br]) \times f_Ie^{-M_I}$$

Here,  $e^{-M_i}$  is the temperature factor related to the amplitude of the atomic vibrations. The calculation of  $M_i$  is presented below.

We first extracted the amplitude and centers of all the peaks. We then obtained the  $A$  coefficient by solving equations S1 and S2, using the intensity of the cubic peaks ( $c(100)$ ,  $c(110)$ ,  $c(111)$  that correspond, respectively, to  $t(110)$ ,  $t(200)$  and  $t(201)$ ). With the  $A$  coefficient found herein (taken as the average of the 3 cubic peaks) and the intensity of the  $t(210)$  peak, we can extract, for each temperature, the value of the structure factor  $F_{t,210}$  using the following formula:

$$|F_{t,210}(T, t)|^2 = \frac{I_{t,210}(T)}{A \cdot p \cdot \left( \frac{1 + \cos^2 2\theta}{\sin^2 \theta \cos \theta} \right)} \quad (\text{S3})$$

where  $p = 8$  for the 210 peak. This gives us the tilt angle by matching with formula S2, that we approximate for small angles as  $F_{t,210} \sim \alpha \cdot t$ . The tilt angle can now be found using:

$$t(T) = \frac{1}{\alpha} \cdot \sqrt{\frac{I_{t,210}(T)}{A \cdot p \cdot \left( \frac{1 + \cos^2 2\theta}{\sin^2 \theta \cos \theta} \right)}} \quad (\text{S4})$$

The result is shown in figure 3a in the main text.

### 3.2 Calculation of the Temperature Factors

The temperature factor  $M_i$  can be extracted from Debye's theory, reported by R.W. James [8]:

$$M_i = \frac{6h^2T}{mk\Theta_{D,i}^2} \left[ \phi(x_i) + \frac{x_i}{4} \right] \left( \frac{\sin \theta}{\lambda} \right)^2 \quad (\text{S5})$$

where  $h$  is the Planck constant,  $T$  is the absolute temperature,  $m$  is the mass of vibrating atoms,  $k$  is the Boltzmann constant,  $\Theta_D$  is the Debye characteristic temperature of the substance,  $x_i = \frac{\Theta_{D,i}}{T}$ ,  $\phi(x) = \frac{1}{x} \int_0^x \frac{\xi}{e^\xi - 1} d\xi \approx 1 + \frac{x^2}{36} - \frac{x^4}{3600} + \dots$ ,  $\theta$  is the Bragg angle (equal to  $\frac{2\theta}{2}$  in the grazing incidence geometry, and  $\lambda$  is the X-ray wavelength.

The Debye temperature for each ion  $i$  in the perovskite structure is taken as  $\Theta_{D,i} = 150$  K, with the influence of the hydrogen atoms neglected.

The temperature factor  $M_i(T)$  has little influence on the calculated tilt. This can be seen in figure S4 that plots the tilt angle for composition  $\text{Cs}_{0.4}\text{FA}_{0.6}\text{Pb}(\text{Br}_{0.17}\text{I}_{0.83})_3$ , calculated for different Debye temperatures.

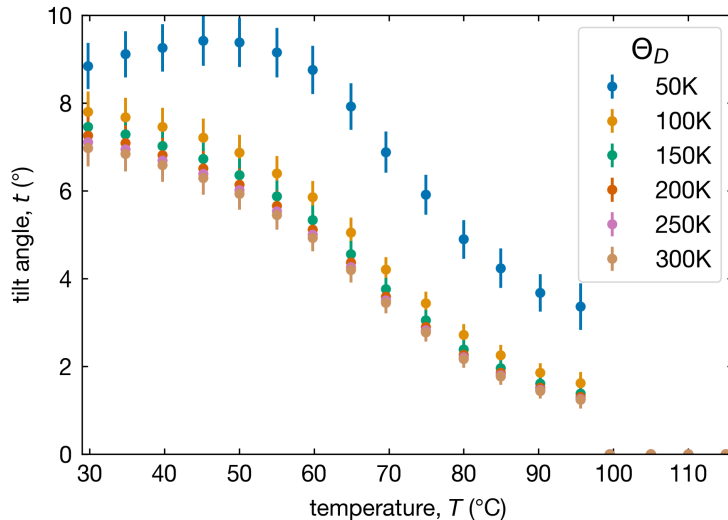


**Figure S4:** Tilt angle calculated for different assumptions of the Debye temperatures.  $\Theta_D$  is considered the same value for all atoms.

### 3.3 Limitations of the method

The methodology described here for the extraction of the tilt angle was used because the assumptions for Rietveld refinement are not necessarily valid for our thin films. Simulated powder diffraction patterns of the respective perovskite composition and tilt angle show that the expected peak intensities differ from those observed in our measurements. We show the result of these simulations in table S1 for a tilt angle of  $7.4^\circ$  (obtained for  $\text{Cs}_{0.4}\text{FA}_{0.6}\text{Pb}(\text{Br}_{0.17}\text{I}_{0.83})_3$  at  $29.8^\circ\text{C}$ , as well as the integrated peak intensities. We note that the  $t(110)/t(001)$  peak at  $q = 1$  is stronger than expected, and the other peaks are somewhat weaker.

**Table S1:** Comparison between simulated pattern and integrated intensity of the experimental peaks after azimuthal integration. Peak intensity is normalised for  $t(110/001)$ .

peak	simulated intensity	integrated intensity
110/001	100	100
111/200	37.5	56.2
210	4.3	4.7
201	10.6	37.8

There is some preferred orientation or crystallographic texture in the XRD pattern that will impact the peak intensity ratios in Table S1. The texture may originate from preferential growth orientation during the film crystallisation. Figure S5a shows an  $I(q, \chi)$  map for  $\text{Cs}_{0.4}\text{FA}_{0.6}\text{Pb}(\text{Br}_{0.17}\text{I}_{0.83})_3$  at  $29.8^\circ\text{C}$ , obtained from the XRD measurement using the PyFAI library [9], illustrating the texture. To make this clearer, we show the azimuthal angle dependence of the integrated intensities of the  $t(110/001)$  and  $t(210)$  peaks in figure S5b. The integration was made from the map in (a), using a Voigt function over a linear background in  $I(q)$  for all values of the azimuthal angle  $\chi$ . This observation may explain the discrepancy shown in table S1. Due to this texture, there is an impact on the exact tilt angles we calculate, but this does not impact our conclusions.

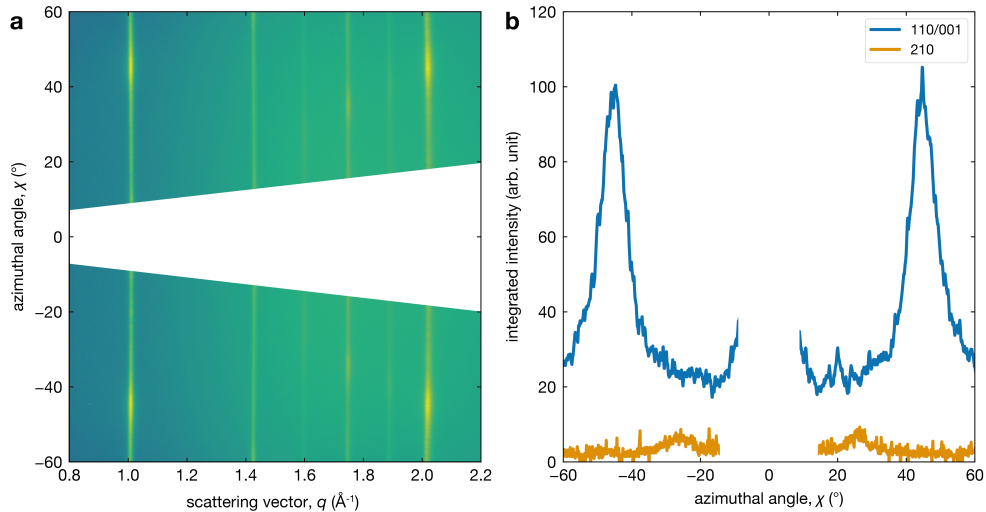


**Figure S5:** Texture of XRD pattern: a)  $I(q, \chi)$  map with  $\chi$  the azimuthal angle (angle with respect to surface normal). Colormap from indigo (low) to yellow (high), b) intensity of the peaks  $t(110/001)$  and  $t(210)$  for composition  $\text{Cs}_{0.4}\text{FA}_{0.6}\text{Pb}(\text{Br}_{0.17}\text{I}_{0.83})_3$  at  $29.8^\circ\text{C}$ . White slab corresponds to the missing wedge where the integration cannot be performed due to the curvature of the Ewald sphere [10].

### Supplementary section 4: Fit of the tilt angle

As explained in the main text, we model the phase transition behavior with a smeared first order or continuous transition. This is because we do not know if the heterogeneity is intrinsic or extrinsic.

A first order phase transition corresponds to a discontinuity in the order parameter (here the tilt angle) that we model with a steplike function, whereas a second-order phase transition can be described by a power law of the form:  $t \sim (T_c - T)^\beta$ , where  $\beta$  is the critical exponent for the phase transition and  $T_c$  the average transition temperature. We convolute both the steplike and the power law dependencies with a Gaussian distribution, to account for the compositional heterogeneity. We fit the temperature dependence of the tilt  $t$  and the Gaussian width with these two convoluted function. Both models are presented in figure S6. We note that it is not possible to distinguish between the first order phase transition and continuous power law on these plots.

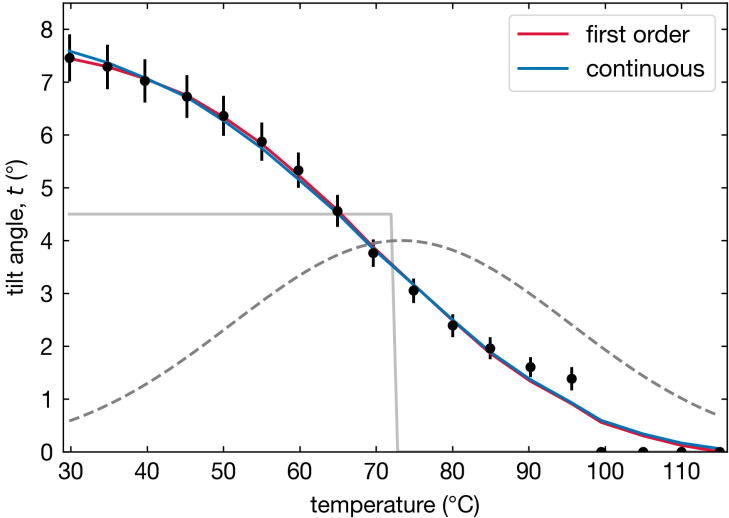


**Figure S6:** Octahedral tilt angle for composition 40-17, fitted with a smeared first order (magenta) and a smeared second order (blue) parameter, that are respectively a step function (shown as a grey solid line) and a power law (not shown), convoluted with a Gaussian (shown as a grey dashed line). The transition width of the Gaussian is about 45 °C

The discontinuity of the step function is the temperature used as the average  $T_c$  in the main text (table 1).

## Supplementary section 5: Lattice parameter behavior

As explained in the main text, unlike pure components where at the phase transition  $a'$  and  $c$  converge to the cubic phase  $d$ , the slightly divergent behavior of lattice constants in  $\text{Cs}_y\text{FA}_{1-y}\text{Pb}(\text{Br}_x\text{I}_{1-x})_3$  originates from the compositional heterogeneity. One simple hypothesis to understand this is to divide the  $\text{Cs}_y\text{FA}_{1-y}\text{Pb}(\text{Br}_x\text{I}_{1-x})_3$  films into four different regions with high Cs-high Br, high Cs-low Br, low Cs-high Br and low Cs-low Br. The phase diagram in the main text (Figure 3c) gives the relative transition temperatures that  $T_{\text{low Cs, high Br}} < T_{\text{low Cs, low Br}} < T_{\text{high Cs, high Br}} < T_{\text{high Cs, low Br}}$ , which is also consistent with the pure component transition temperatures, *i.e.*  $\text{FAPbBr}_3$ ,  $\text{FAPbI}_3$ ,  $\text{CsPbBr}_3$  and  $\text{CsPbI}_3$  [11, 12, 13].

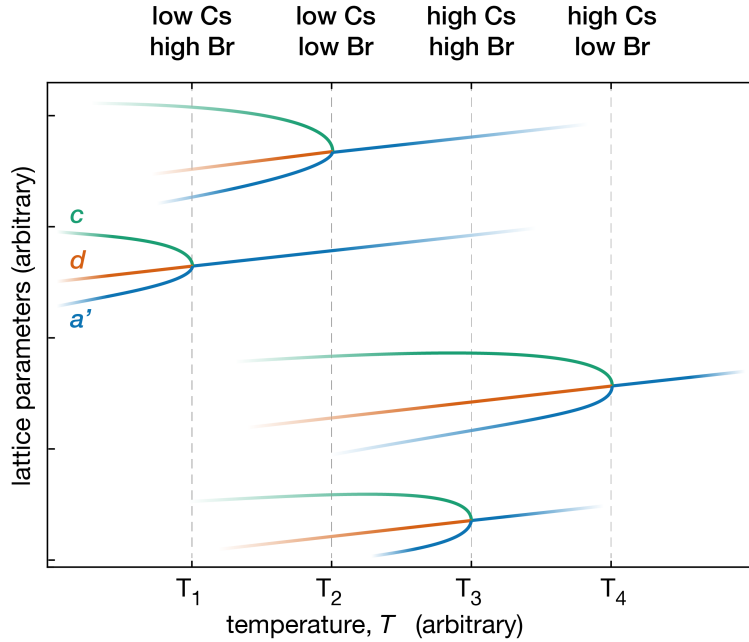


**Figure S7:** Diagram for the proposed evolution of the lattice parameters with different concentrations with four different tetragonal-to-cubic phase transitions ( $T_1$ – $T_4$ ). The mixed composition would have a phase transition behavior broadened from  $T_1$  (phase transition temperature for the low Cs, high Br compound) to  $T_4$  (phase transition temperature for the high Cs, low Br compound)

This is schematically shown in Figure S7. As the temperature increases, these four regions transform into the cubic phase according to their own transition temperature and their lattice parameters have the same convergent behavior as pure compounds. Since our measured lattice constants from  $t(210)$  and  $t(201)$  only reflect regions of the film in the tetragonal phase, lattice parameters in the region that transform first (as temperature is increased) will not be averaged into the results in Figure 4 of the main text. Thus, the lattice parameters  $a'$  and  $c$  shown in Figure 4 of the main text are those from regions that remain tetragonal as temperature increases. We can use Figure S7, which is a qualitative plot of the variation of  $a'$  and  $c$  for several possible compositional variations, to obtain some insight into the composition variations. Figure 4 in main text shows that as temperature increases close to  $T_0$ ,  $a'$  decreases and  $c$  increases markedly. In Figure S7, this corresponds to temperature increasing above  $T_1$ . Since  $c$  significantly increases, this suggests that the composition of

the tetragonal regions above T1 has a lower Br concentration than the average (larger  $c$ ), with likely some regions of locally high Cs (smaller  $a'$ ). Without a more refined model that is beyond the scope of the present paper, quantitative analysis for region composition is not possible.

### Supplementary section 6: EQE

The EQE is recorded between 300 and 800 nm. To find the band gap, we start by fitting the low energy onset of the EQE with an error function (shown as a blue curve in figure S8. We extract the bandgap from the intersection of the tangent (shown as an orange line in figure S8 to this error function at the center (point of higher variation of the error function), with a linear fit taken for the 4 points with the highest wavelength.

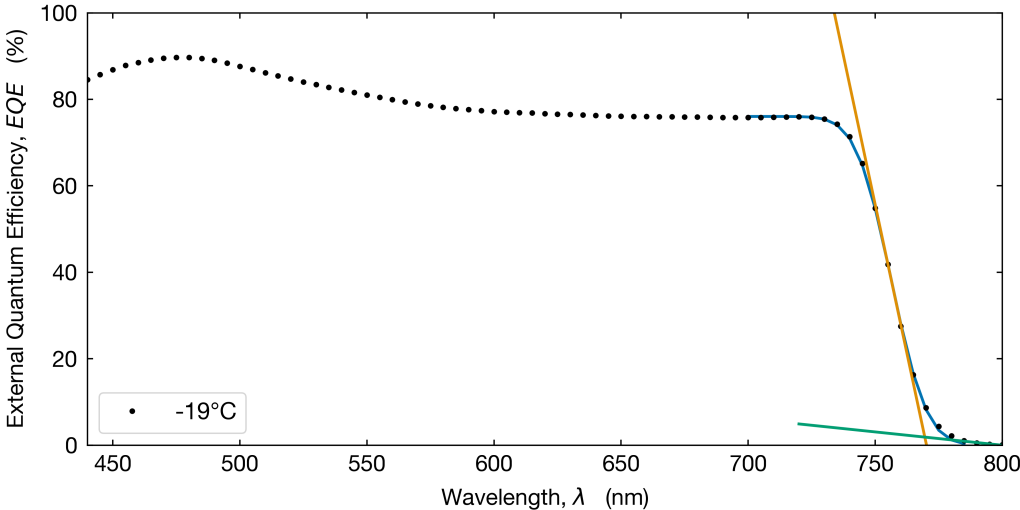


**Figure S8:** example of the EQE at  $-19^\circ\text{C}$  (black dots) with an error-function fit on the low-energy onset (blue curve). The orange curve shows the tangent in the center of this error function. The green curve shows a linear fit of the 4 points of higher wavelength  $\lambda$ .

## Supplementary References

1. Beal RE, Hagström NZ, Barrier J, Gold-Parker A, Prasanna R, Bush KA, Pasarello D, Schelhas L, Brüning K, Steinrück HG, McGehee MD, Toney MF, and Nogueira AF. Structural origins of light-induced phase segregation in organic-inorganic halide perovskite photovoltaic materials. *Matter* 2020; 2:1–13. DOI: 10.1016/j.matt.2019.11.001
2. Kieslich G, Sun S, and Cheetham AK. Solid-state principles applied to organic-inorganic perovskites: new tricks for an old dog. *Chemical Science* 2014; 5(12):4712–5. DOI: 10.1039/c4sc02211d
3. Kieslich G, Sun S, and Cheetham AK. An extended Tolerance Factor approach for organic-inorganic perovskites. *Chemical Science* 2015; 6(6):3430–3. DOI: 10.1039/C5SC00961H
4. Goldschmidt VM. Die Gesetze der Kristallochemie. *Naturwissenschaften* 1926; 14:477–85. DOI: 10.1007/BF01507527
5. Ouyang R, Curtarolo S, Emre A, Scheffler M, and Ghiringhelli LM. SISSO: A compressed-sensing method for identifying the best low-dimensional descriptor in an immensity of offered candidates. *Physical Review Materials* 2018; 2:083802. DOI: 10.1103/PhysRevMaterials.2.083802
6. Bartel CJ, Sutton C, Goldsmith BR, Ouyang R, Musgrave CB, Ghiringhelli LM, and Scheffler M. New tolerance factor to predict the stability of perovskite oxides and halides. *Science Advances* 2019; 5:eaav0693. DOI: 10.1126/sciadv.aav0693
7. Newville M, Otten R, Nelson A, Ingargiola A, Stensitzki T, Allan D, Fox A, Carter F, Michał, Pustakhod D, Ram Y, Glenn, Deil C, Stuermer, Beelen A, Frost O, Zobrist N, Mark, Pasquevich G, Hansen ALR, Spillane T, Caldwell S, Polloreno A, Andrewhanum, Fraine J, deep-42-thought, Maier BF, Gamari B, Persaud A, and Almaraz A. *lmfit/lmfit-py* 1.0.1. Version 1.0.1. 2020 May. DOI: 10.5281/zenodo.3814709. Available from: <https://doi.org/10.5281/zenodo.3814709>
8. James RW. *The Optical Principles of the Diffraction of X-Rays*. London: G. Bell and Sons, 1948. Chap. V. The Influence of Temperature on the Diffraction of X-rays by Crystals
9. Kieffer J and Karkoulis D. PyFAI, a versatile library for azimuthal regrouping. *Journal of Physics: Conference Series*. IOP Publishing, 2013 :202012. DOI: 10.1088/1742-6596/425/20/202012i
10. Baker JL, Jimison LH, Mannsfeld S, Volkman S, Yin S, Subramanian V, Salleo A, Alivisatos AP, and Toney MF. Quantification of thin film crystallographic orientation using X-ray diffraction with an area detector. *Langmuir* 2010; 26:9146–51. DOI: 10.1021/1a904840q
11. Keshavarz M, Ottesen M, Wiedmann S, Wharmby M, Kuchler R, Yuan H, Debroye E, Steele JA, Martens J, Hussey NE, Bremholm M, Roeffaers MBJ, and Hofkens J. Tracking Structural Phase Transitions in Lead-Halide Perovskites by Means of Thermal Expansion. *Advanced Materials* 2019 Apr :1900521. DOI: 10.1002/adma.201900521
12. Näsström H, Becker P, Márquez JA, Shargaieva O, Mainz R, Unger E, and Unold T. Dependence of phase transitions on halide ratio in inorganic CsPb(BrxI1-x)3 perovskite thin films obtained from high-throughput experimentation. *Journal of Materials Chemistry A* 2020; 8:22626–31. DOI: 10.1039/d0ta08067e
13. Chen T, Foley BJ, Park C, Brown CM, Harriger LW, Lee J, Ruff J, Yoon M, Choi JJ, and Lee SH. Entropy-driven structural transition and kinetic trapping in formamidinium lead iodide perovskite. *Science Advances* 2016 Oct; 2:e1601650. DOI: 10.1126/sciadv.1601650